Tuning the supercurrent distribution in parallel ballistic graphene Josephson junctions

Philipp Schmidt[1,2,*] Luca Banszerus[1,2] Benedikt Frohn,[1] Stefan Blien[3] Kenji Watanabe[4]
Takashi Taniguchi[5] Andreas K. Hüttel[3] Bernd Beschoten[1] Fabian Hassler[6] and
Christoph Stampfer[1,2]

[1]*JARA-FIT and 2nd Institute of Physics, RWTH Aachen University, Aachen 52074, Germany*
[2]*Peter Grünberg Institute (PGI-9), Forschungszentrum Jülich, Jülich 52425, Germany*
[3]*Institute for Experimental and Applied Physics, University of Regensburg, Regensburg 93040, Germany*
[4]*Research Center for Functional Materials, National Institute for Materials Science, 1-1 Namiki, Tsukuba 305-0044, Japan*
[5]*International Center for Materials Nanoarchitectonics, National Institute for Materials Science, 1-1 Namiki, Tsukuba 305-0044, Japan*
[6]*JARA-Institute for Quantum Information, RWTH Aachen University, Aachen 52056, Germany*

We report on a ballistic and fully tunable Josephson-junction system consisting of two parallel ribbons of graphene in contact with superconducting molybdenum-rhenium. By electrostatic gating of the two individual graphene ribbons, we gain control over the real-space distribution of the superconducting current density, which can be continuously tuned between the two ribbons. We extract the respective gate-dependent spatial distributions of the real-space current density by employing Fourier and Hilbert transformations of the magnetic-field-induced modulation of the critical current. This approach is fast and does not rely on a symmetric current profile. It is therefore a universally applicable tool, potentially useful for carefully adjusting Josephson junctions.

Josephson junctions [1], which consist of two superconductors connected by a normal-conducting material or an insulator, have been investigated for a long time, since they can be used for infrared detectors [2], ultrafast logic circuits [3], or sensitive magnetic flux and voltage measurements [4]. Additionally, Josephson junctions are a powerful tool for exploring the properties of superconductors by connecting the supercurrent to the phase of the macroscopic wave function [5]. In the last decade, Josephson junctions have also been employed as building blocks for superconducting quantum computing [6–8].

Substituting the normal conductor or insulator with graphene as the weak link leads to highly tunable Josephson junctions with transparent interfaces due to the absence of a Schottky barrier [9]. In the past, graphene-based Josephson junctions [10–23] have been investigated by tunneling spectroscopy [24,25] and have been used to study crossed Andreev reflection [26] and superconductivity in the quantum Hall regime [27–30]. Besides the magnitude of the supercurrent carried over the Josephson junction, the spatial current distribution has been analyzed in the case of edge currents in graphene [31–33]

and for studying topological Josephson junctions [34]. Furthermore, the control and determination of the current density is important for the operation of protected Josephson rhombus chains [35] or protected superconducting qubits based on tunable Josephson interferometer arrays [36]. Here, the pairwise balance of the Josephson junctions protects the qubit against detuning or noise. However, the real-space current density is not directly accessible in electrical transport measurements.

To obtain the real-space current density of two coupled Josephson junctions, an out-of-plane magnetic field has to be applied to the junction, which leads to a modulation of the critical current. This can be expressed as the magnitude of a Fourier transform of the real-space current density, which, thus, can be reconstructed from the modulation of the critical current by an inverse Fourier transform [37,38]. Even though this method has been recently applied to a gated epitaxial Al-InAs Josephson junction [39], highly nonsymmetric cases have not been studied so far. In this work, we study a fully tunable graphene double Josephson junction formed by two parallel ribbons with superconducting molybdenum-rhenium ($Mo_{30}Re_{70}$) contacts. By using both top and back gates, we can independently tune the supercurrent distribution between the two

---

*philipp.schmidt3@rwth-aachen.de

ribbons. We present results based on a reconstruction of the supercurrent from the magnetic-field-dependent critical current using a combination of Fourier and Hilbert transformations, which allows one to extract the asymmetric supercurrent distribution.

A schematic and an optical micrograph of our device are shown in Fig. 1(a). The device consists of graphene grown by chemical vapor deposition (CVD), which is encapsulated in hexagonal boron nitride (h-BN) crystals by dry-transfer van der Waals stacking [40–42]. The stack is etched into two parallel ribbons by $CF_4 + O_2$ reactive ion etching through a poly(methyl methacrylate) resist mask, which has been patterned by standard electron-beam lithography to a width of $w = 1.1$ µm with a separation of $\delta = 0.2$ µm between the two ribbons. The graphene is electrically contacted to superconducting Mo-Re electrodes, fabricated by sputter deposition defining the junction length of $L = 0.3$ µm. Separated by a 300-nm SiO_2 gate dielectric, the device is placed on a highly doped silicon substrate acting as a back gate. Additionally, a gold top gate is deposited onto one of the graphene ribbons, while the whole device is protected by an insulating layer of Al_2O_3 grown by atomic layer deposition.

All this allows us to tune the charge carrier density of the two graphene ribbons independently, since one of them is affected only by the back gate (BG), leading to a charge carrier density of $n_1 = \alpha_{BG}(V_{BG} - V^0_{BG})$, while the other ribbon is tuned by the combination of both top-gate (TG) and back-gate voltages, $n_2 = \alpha_{BG}(V_{BG} - V^0_{BG}) + \alpha_{TG}(V_{TG} - V^0_{TG})$, where α_{BG} and α_{TG} are the respective gate lever arms, which are proportional to the capacitive coupling of the respective gate to the graphene. The gate settings $V^0_{BG} = -1.3$ V and $V^0_{TG} = -0.25$ V account for a constant shift of the charge neutrality point, and the gate lever arms are estimated to be $\alpha_{BG} = 7.0 \times 10^{10}$ V^{-1} cm^{-2} and $\alpha_{TG} = 4.9 \times 10^{10}$ V^{-1} cm^{-2}. With this individual gate tuning, the device can be tuned into four regimes defined by the polarities of the two ribbons [see Fig. 1(b)]: $p|n$ (1), $n|n$ (2), $p|p$ (3), and $n|p$ (4). All measurements were performed in a He^3/He^4 dilution refrigerator with a base temperature of around 10 mK. A constant parasitic resistance of $R_0 = 2.55$ kΩ arises from the wiring and the filters.

In Fig. 1(c) we show the differential conductance dI/dV of the device as a function of the current I and charge carrier density n_2, which is tuned by the top-gate voltage, while the back-gate voltage is set to the charge neutrality point ($V_{BG} = -1.3$ V). A superconducting regime (yellow color) is present symmetrically around $I = 0$ for both electron ($n > 0$) and hole ($n < 0$) doping and can be distinguished from the normal-conducting regime at larger current values. The current at which the transition between these two regimes occurs defines the critical current I_c. Here it is important to note that no influence of the current sweep direction on the critical current has been observed.

Oscillations of the differential conductance and the critical current that are observed in the p-doped region ($n < 0$) can be attributed to Fabry-Perot (FP) interference [43,44]. They originate from the $\tilde{n}$-p-$\tilde{n}$ graphene cavity in the double-gated ribbon, which is formed by the Mo-Re yielding a highly local $\tilde{n}$ doping in the graphene near the contacts [see Fig. 1(b)]. The critical current becomes largest for n doping ($n > 0$) since there is no p-$\tilde{n}$ junction, which increases the resistance. Since the carrier density is only weakly tuned in the outer graphene parts next to the Mo-Re contacts, there is no cavity formed, as seen by the suppression of FP oscillations in this regime.

The FP oscillations are further explored in Fig. 1(d), where we plot the normal state conductance, measured at a bias voltage of 1 mV to keep the junction in the normal state regime, at fixed back-gate voltage and varying top-gate voltage. Analyzing the FP oscillations (see Supplemental Material [45] for details) for both ribbons results in an extracted cavity length of $L_1 = 314 \pm 50$ nm and $L_2 = 335 \pm 15$ nm, which fit well to the lithographic length of the channel (see inset in Fig. 1(d) for sample dimensions), in agreement with ballistic and phase coherent transport.

In Fig. 1(e), we show the normal state conductance of the device as a function of top- and back-gate voltages. The four possible doping configurations sketched in Fig. 1(b) can be identified [see labels in Figs. 1(e) and 1(f)]. The top-gate voltage only changes the charge carrier density of the respective graphene ribbon underneath, while the back-gate voltage influences both ribbons. Configuration (1) refers to the situation of a $\tilde{n}$-p-$\tilde{n}$ junction in one ribbon, while the other (underneath the top gate) is completely n-doped. The complementary configuration, denoted as configuration (4), has the $\tilde{n}$-p-$\tilde{n}$ junction underneath the top gate. Configuration (3) refers to the case of both ribbons tuned to a $\tilde{n}$-p-$\tilde{n}$ junction. Here, a combination of the FP oscillations by the two gates can be seen. Finally, configuration (2) describes the case of unipolar n-type doping for both ribbons and thus the absence of any p-$\tilde{n}$ junctions, which results in an enhanced conductance.

Reducing the bias voltage and thus entering the superconducting state enables us to extract the critical current I_c. The critical current is plotted as a function of top- and back-gate voltages in Fig. 1(f). The map resembles most features of the conductance map in Fig. 1(e). Combining the critical current and the normal state resistance gives an I_cR_N product between 30 and 60 µV, comparable to results in the literature [19].

Next we focus on the magnetic field dependence of the critical current, which will allow the reconstruction of its spatial distribution. We measure the differential conductance while varying both the current I and the out-of-plane magnetic field B_z. The magnetic field induces a phase difference between the two bulk superconductors, leading
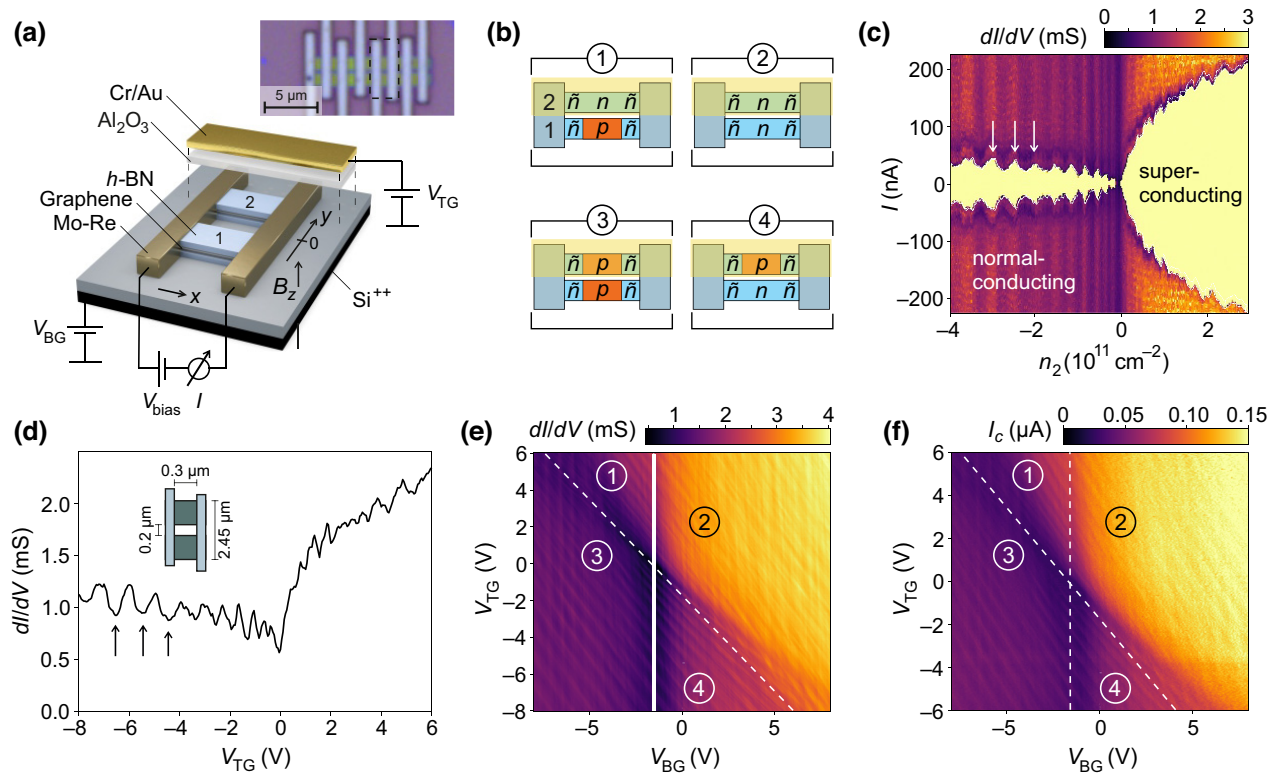
FIG. 1. (a) Schematic of the device structure and optical micrograph of the device. Two etched graphene ribbons (1 and 2) encapsulated in h-BN are contacted with superconducting Mo-Re. In addition to the global Si^{++} back gate, a Cr/Au top gate is deposited onto one of the ribbons (not shown in the micrograph), separated by a layer of aluminum oxide (Al_2O_3). A constant bias voltage V_{bias} is applied and the resulting current I is measured. (b) Schematic of the doping configurations accessible with the two gates. The Mo-Re contacts induce a persistent $\tilde{n}$ doping at their graphene interfaces. (c) Differential conductance as a function of charge carrier density n_2 in the top-gated graphene ribbon and current ($T \approx 10$ mK). The superconducting regime around $I = 0$ is well visible. For p doping, i.e., $n < 0$, Fabry-Perot oscillations (see vertical arrows) are visible in the critical current. (d) Normal state conductance as a function of top-gate voltage V_{TG} with reference to the charge neutrality point. The Fabry-Perot oscillations are also marked by arrows. The inset shows a sketch of the device with the relevant dimensions. (e) The normal state conductance versus applied top- and back-gate voltages showing four electrostatic doping regimes of the graphene ribbons. The white vertical line corresponds to the position of the line trace shown in panel (d). (f) The gate-dependent critical currents show a tuning similar to the normal state conductance in panel (e).

to a modulation of the critical current I_c [46] as shown in Fig. 2(a) for the case of one graphene ribbon being conductive ($\tilde{n}$-n-$\tilde{n}$) while the other is tuned near the charge neutrality point ($\tilde{n}$-0-$\tilde{n}$) [see inset of Fig. 2(b)].

To gain information on the real-space superconducting current density distribution, j_c, we perform an inverse Fourier transformation of the extracted $I_c(B)$ combined with a Hilbert transformation to reconstruct the phase of the signal as introduced by Dynes and Fulton [37] (see Supplemental Material [45] for details). Note that the reconstructed data leave freedom for an arbitrary offset in the position y together with the sign of y (which corresponds to mirroring around $y = 0$). We correct the reconstructed data such that position $y = 0$ corresponds to the center of the two graphene ribbons and flip the y axis such that the major peak corresponds to the ribbon with the larger conductance. Here, the junction tuned by the back gate only is located at negative position ($y < 0$) whereas

the top-gated junction is located at positive position ($y > 0$).

The extracted current density distribution in Fig. 2(b) of the measurement shown in Fig. 2(a) visualizes the asymmetric supercurrent distribution in this configuration with the largest critical currents along the ($\tilde{n}$-n-$\tilde{n}$) ribbon at $y > 0$. Changing the gate voltages to the symmetric configuration [see configuration (3) in Fig. 1(b)], where both graphene ribbons are p-doped, shows a different modulation pattern [see Fig. 2(c)] and the extracted supercurrent density indeed shows an even current distribution between the two ribbons [see Fig. 2(d)]. We use the width of these current peaks to adapt the y axis of the reconstructed data to $y = \Phi_0/(Bt_B)$ with the magnetic flux quantum $\Phi_0 = h/(2e)$ and $t_B = L + \lambda_1 + \lambda_2$. Taking into account the length obtained by the analysis of FP oscillations of $L = 335$ nm results in a London penetration depth of $\lambda_{1/2} \approx 330$ nm.
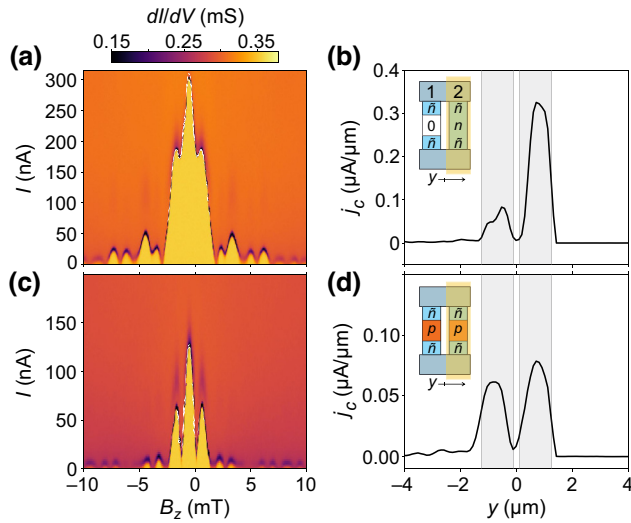
FIG. 2.   (a) Differential conductance as a function of current and out-of-plane magnetic field for the gating configuration of one conductive, n-doped graphene ribbon while the other is tuned to charge neutrality [see inset of panel (b)]. The critical current shows a Fraunhofer-like modulation pattern. (b) The extracted real-space current density confirms the expected asymmetric current distribution by the pronounced peak at $y > 0$. (c) Differential conductance map for the case where both ribbons are p-doped. The magnetic-field-induced modulation of the critical current changes to a more superconducting-quantum-interference-device-like behavior. (d) The resulting real-space current density shows two peaks with almost equal intensities, proving the symmetric current distribution in the two ribbons.

To measure the critical current directly instead of extracting it from multidimensional measurements, we used a home-built circuit which detects the peak in differential resistance when sweeping the applied current (see Supplemental Material [45] for details). This allows an enhanced measurement speed by a factor of 60 and opens the door to measure the modulation patterns as a function of the applied gate voltages. In Fig. 3(a), we show the logarithm of the critical current as a function of magnetic field and V_{BG}. Again, the magnetic-field-induced modulation which depends on the applied back-gate voltage is visible by the features of brighter colors. Even the modulation features of low intensity at higher magnetic fields can be seen.

Strikingly, the critical current is lower for negative back-gate voltages, because of the resulting $\tilde{n}$-p-$\tilde{n}$ junction, which increases the normal resistance, which is less pronounced for positive voltages. We perform the reconstruction for each line and show the gate-dependent real-space current distribution in Fig. 3(b). The most important features are the two distinctive areas with high current densities at $y \approx \pm 1$ μm, which correspond to the two graphene ribbons. It can be seen that the back gate indeed tunes both junctions and thus changes the current densities
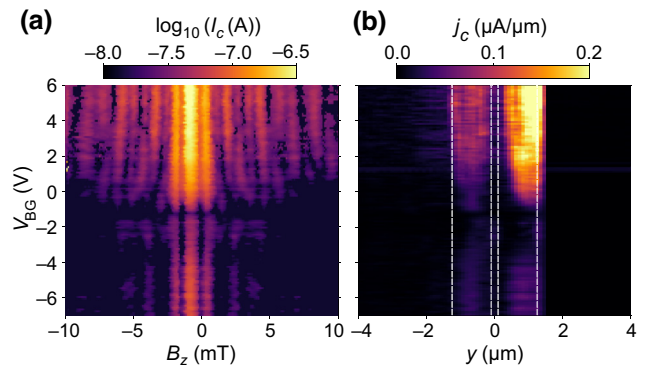

FIG. 3.   (a) Modulation of the critical current (in logarithmic scale) as a function of out-of-plane magnetic field and back-gate voltage at fixed $V_{TG} = 6.3$ V. The modulation pattern changes with applied gate voltage. (b) Line-wise reconstruction from the data in panel (a) resulting in the real-space position and gate-voltage-dependent superconducting current density distribution. The current density shows a nonsymmetric distribution as well as a symmetrical influence of the back gate on the two graphene ribbons.

for the areas at $y < 0$ and $y > 0$. The asymmetry is caused by the top gate influencing only ribbon 2 [see Figs. 1(a) and 1(b)].

We now focus on the real-space superconducting current densities for different electrostatic configurations in more detail. In the first configuration, presented in Fig. 4(a), most current flows through ribbon 1 which is not covered by the top gate at $y < 0$. In Fig. 4(a) the superconducting current density is plotted as a function of real-space position and back-gate voltage. The back-gate voltage tunes the bulk of ribbon 1 from n doping at $V_{BG} > 0$ to p doping, resulting in a $\tilde{n}$-p-$\tilde{n}$ configuration at $V_{BG} < 0$, while the fixed top-gate voltage keeps the bulk of ribbon 2 for all V_{BG} values p-doped (i.e., in the $\tilde{n}$-p-$\tilde{n}$ configuration), as shown by the inset in Fig. 4(a). The map shows two vertical features of high current density that can be assigned to the supercurrents running through the two ribbons. The highest current density is present in the case of n doping ($V_{BG} > 0$) for $y < 0$, resulting from the higher normal conductance of the $\tilde{n}$-n-$\tilde{n}$ ribbon.

In Fig. 4(b) we show a line cut along the dashed line in Fig. 4(a) where the asymmetry is well visible as the peak at $y < 0$ is more pronounced. Additionally, line traces of the current density as a function of V_{BG} extracted at the center positions of the two ribbons [see blue and red triangles in Fig. 4(a)] are shown in Fig. 4(c). While ribbon 1 (blue trace) shows a clear transition from reduced current density with FP oscillations at $V_{BG} < 0$ to an increasing current density for $V_{BG} > 0$, ribbon 2 (red trace) shows FP oscillations even for positive V_{BG} values (see black arrows). This gives us an unambiguous way to identify the peaks in the current density as the junction with or without top gate.
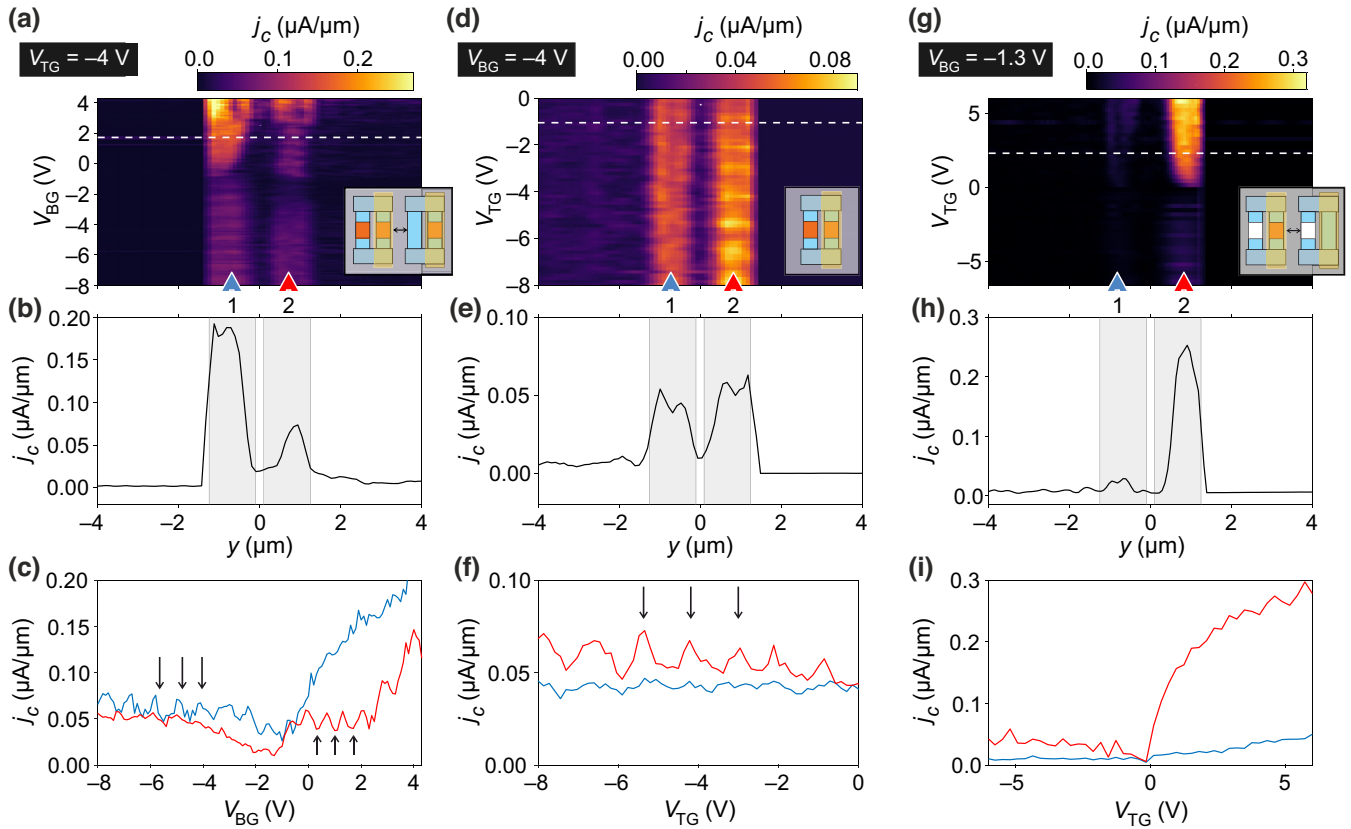
FIG. 4. (a) Superconducting current density as a function of real-space position and back-gate voltage for a doping configuration where both ribbons are tuned by the back gate with fixed top-gate voltage. The inset illustrates the respective doping configuration changing from $p|p$ to $n|p$ with increasing gate voltage. (b) Line profile of the superconducting current density along the white dashed line in panel (a). The asymmetric current distribution between the two ribbons can be well identified. The gray areas correspond to the lithographically defined positions of the graphene ribbons 1 and 2. (c) Line profiles of the current densities along the gate axis at the left and right junctions indicated by blue and red triangles in panel (a), respectively. The Fabry-Perot oscillations, marked by the black arrows, can also be seen in the current density. (d)–(f) Similar to (a)–(c) but where the top-gate voltage is varied while both ribbons are p-doped, leading to a symmetric current distribution. (g)–(i) Similar as (d)–(f) but ribbon 1 is tuned to the charge neutrality point. Therefore, almost all the current flows through ribbon 2, leading to a highly asymmetric current distribution.

A similar analysis is performed for the configuration where we fix V_{BG} and tune V_{TG} so that both graphene ribbons are p-doped [see Figs. 4(d)–4(f)]. Here, the position-dependent current density [Fig. 4(d)] show a rather symmetric distribution between the two ribbons visualized by the two parallel vertical strips of high current density for all measured top-gate voltages. The even distribution can also be seen in the line cut at $V_{TG} \approx -1$ V [see Fig. 4(e)]. Moreover, we observe an oscillatory modulation of the real-space current density with respect to the gate voltage due to FP interference in the $\tilde{n}$-p-$\tilde{n}$ cavity. This effect becomes more visible in the gate-dependent line cuts at the position of the two ribbons, as indicated by the vertical arrows [see Fig. 4(f)]. In this configuration, the FP oscillation is only present for the ribbon underneath the top gate (ribbon 2), since V_{BG} is kept constant, and thus the tuning of charge carrier density leading to the FP oscillation is asymmetric.

Finally, in Figs. 4(g)–4(i) we show a third configuration where only the graphene ribbon underneath the top gate is conductive, while the other is tuned to its charge neutrality point by the back gate. Consequently, the extracted current density shows a highly asymmetric distribution among the ribbons with almost no supercurrents at $y < 0$ [see Fig. 4(g)]. This also becomes clear in the line cut at $V_{TG} \approx 2.4$ V [Fig. 4(h)], where only one significant peak at $y > 0$ can be identified. Furthermore, the current suppression in the case of a $\tilde{n}$-p-$\tilde{n}$ junction can be seen in Fig. 4(i) when comparing the current density at negative and positive gate voltages. This fits well to the observed difference in critical current for n and p doping [compare to Fig. 1(f)].

In summary, we have presented a fully tunable graphene-based double Josephson junction consisting of two parallel graphene ribbons contacted by Mo-Re. We showed a remarkable control over these junctions and are able to individually tune the charge carrier densities of both

ribbons. This allows us to continuously control the distribution of the superconducting current density in the two ribbons independently. Through ballistic transport, ensured by the dry-transfer fabrication method of the device, we were able to observe FP oscillations. From these oscillations, we could determine the length of the electrostatic $\tilde{n}$-p-$\tilde{n}$ cavity between the superconducting contacts.

In order to test the tuning capabilities of the graphene Josephson junction, we measured the critical current depending on magnetic field and gate voltages, leading to the magnetic-field-induced modulation of the critical current. Most interestingly, we could map the current density distributions in real space of the individual graphene ribbons, highlighting the FP oscillations present in the individual ribbons and proving the excellent gate tunability of the junctions from an even to a fully asymmetric current distribution. This opens the door to controlling and monitoring the current densities in complex Josephson interferometer circuits, potentially leading to protected superconducting qubits [36].

The data supporting the findings are available in a Zenodo repository under accession code [48].

[1] B. Josephson, Possible new effects in superconductive tunnelling, Phys. Lett. **1**, 251 (1962).

[2] E. D. Walsh, D. K. Efetov, G.-H. Lee, M. Heuck, J. Crossno, T. A. Ohki, P. Kim, D. Englund, and K. C. Fong, Graphene-based Josephson-junction single-photon detector, Phys. Rev. Appl. **8**, 024022 (2017).

[3] P. Bunyk, K. Likharev, and D. Zinoviev, RSFQ technology: Physics and devices, Int. J. High Speed Electron. Syst. **11**, 257 (2001).

[4] M. Grundmann, in *Encyclopedia of Condensed Matter Physics*, edited by F. Bassani, G. L. Liedl, and P. Wyder (Elsevier, Oxford, 2005), p. 17.

[5] R. Gross, A. Marx, and F. Deppe, *Applied Superconductivity: Josephson Effect and Superconducting Electronics*, De

Gruyter Textbook Series (Walter De Gruyter Incorporated, Berlin, 2016).

[6] H.-L. Huang, D. Wu, D. Fan, and X. Zhu, Superconducting quantum computing: A review, Sci. China Inf. Sci. **63**, 1 (2020).

[7] M. Kjaergaard, M. E. Schwartz, J. Braumüller, P. Krantz, J. I.-J. Wang, S. Gustavsson, and W. D. Oliver, Superconducting qubits: Current state of play, Annu. Rev. Condens. Matter Phys. **11**, 369 (2020).

[8] A. Blais, A. L. Grimsmo, S. M. Girvin, and A. Wallraff, Circuit quantum electrodynamics, Rev. Mod. Phys. **93**, 025005 (2021).

[9] V. E. Calado, S. Goswami, G. Nanda, M. Diez, A. R. Akhmerov, K. Watanabe, T. Taniguchi, T. M. Klapwijk, and L. M. K. Vandersypen, Ballistic Josephson junctions in edge-contacted graphene, Nat. Nanotechnol. **10**, 761 (2015).

[10] C. T. Ke, I. V. Borzenets, A. W. Draelos, F. Amet, Y. Bomze, G. Jones, M. Craciun, S. Russo, M. Yamamoto, S. Tarucha, and G. Finkelstein, Critical current scaling in long diffusive graphene-based Josephson junctions, Nano Lett. **16**, 4788 (2016).

[11] I. V. Borzenets, F. Amet, C. T. Ke, A. W. Draelos, M. T. Wei, A. Seredinski, K. Watanabe, T. Taniguchi, Y. Bomze, M. Yamamoto, S. Tarucha, and G. Finkelstein, Ballistic Graphene Josephson Junctions from the Short to the Long Junction Regimes, Phys. Rev. Lett. **117**, 237002 (2016).

[12] H. B. Heersche, P. Jarillo-Herrero, J. B. Oostinga, L. M. K. Vandersypen, and A. F. Morpurgo, Bipolar supercurrent in graphene, Nature **446**, 56 (2007).

[13] X. Du, I. Skachko, and E. Y. Andrei, Josephson current and multiple Andreev reflections in graphene SNS junctions, Phys. Rev. B **77**, 184507 (2008).

[14] C. Ojeda-Aristizabal, M. Ferrier, S. Guéron, and H. Bouchiat, Tuning the proximity effect in a superconductor-graphene-superconductor junction, Phys. Rev. B **79**, 165436 (2009).

[15] I. V. Borzenets, U. C. Coskun, S. J. Jones, and G. Finkelstein, Phase Diffusion in Graphene-Based Josephson Junctions, Phys. Rev. Lett. **107**, 137005 (2011).

[16] K. Komatsu, C. Li, S. Autier-Laurent, H. Bouchiat, and S. Guéron, Superconducting proximity effect in long superconductor/graphene/superconductor junctions: From specular Andreev reflection at zero field to the quantum Hall regime, Phys. Rev. B **86**, 115412 (2012).

[17] N. Mizuno, B. Nielsen, and X. Du, Ballistic-like supercurrent in suspended graphene Josephson weak links, Nat. Commun. **4**, 1 (2013).

[18] J.-H. Choi, G.-H. Lee, S. Park, D. Jeong, J.-O. Lee, H.-S. Sim, Y.-J. Doh, and H.-J. Lee, Complete gate control of supercurrent in graphene p–n junctions, Nat. Commun. **4**, 1 (2013).

[19] T. Li, J. Gallop, L. Hao, and E. Romans, Ballistic Josephson junctions based on CVD graphene, Supercond. Sci. Technol. **31**, 045004 (2018).

[20] D. A. Manjarrés, S. Gómez Páez, and W. J. Herrera, Skewness and critical current behavior in a graphene Josephson junction, Phys. Rev. B **101**, 064503 (2020).

[21] G. Nanda, J. L. Aguilera-Servin, P. Rakyta, A. Kormányos, R. Kleiner, D. Koelle, K. Watanabe, T. Taniguchi, L. M. K. Vandersypen, and S. Goswami, Current-phase relation

of ballistic graphene Josephson junctions, Nano Lett. **17,** 3396 (2017).

[22] C. D. English, D. R. Hamilton, C. Chialvo, I. C. Moraru, N. Mason, and D. J. Van Harlingen, Observation of non-sinusoidal current-phase relation in graphene Josephson junctions, Phys. Rev. B **94,** 115435 (2016).

[23] G.-H. Lee and H.-J. Lee, Proximity coupling in superconductor-graphene heterostructures, Rep. Prog. Phys. **81,** 056502 (2018).

[24] L. Bretheau, J. I.-J. Wang, R. Pisoni, K. Watanabe, T. Taniguchi, and P. Jarillo-Herrero, Tunnelling spectroscopy of Andreev states in graphene, Nat. Phys. **13,** 756 (2017).

[25] J. I.-J. Wang, L. Bretheau, D. Rodan-Legrain, R. Pisoni, K. Watanabe, T. Taniguchi, and P. Jarillo-Herrero, Tunneling spectroscopy of graphene nanodevices coupled to large-gap superconductors, Phys. Rev. B **98,** 121411 (2018).

[26] G.-H. Park, K. Watanabe, T. Taniguchi, G.-H. Lee, and H.-J. Lee, Engineering crossed Andreev reflection in double-bilayer graphene, Nano Lett. **19,** 9002 (2019).

[27] P. Rickhaus, M. Weiss, L. Marot, and C. Schönenberger, Quantum Hall effect in graphene with superconducting electrodes, Nano Lett. **12,** 1942 (2012).

[28] A. W. Draelos, M. T. Wei, A. Seredinski, C. T. Ke, Y. Mehta, R. Chamberlain, K. Watanabe, T. Taniguchi, M. Yamamoto, S. Tarucha, I. V. Borzenets, F. Amet, and G. Finkelstein, Investigation of supercurrent in the quantum Hall regime in graphene Josephson junctions, J. Low Temp. Phys. **191,** 288 (2018).

[29] L. Zhao, E. G. Arnault, A. Bondarev, A. Seredinski, T. F. Q. Larson, A. W. Draelos, H. Li, K. Watanabe, T. Taniguchi, F. Amet, H. U. Baranger, and G. Finkelstein, Interference of chiral Andreev edge states, Nat. Phys. **16,** 862 (2020).

[30] Ö. Gül, Y. Ronen, S. Y. Lee, H. Shapourian, J. Zauberman, Y. H. Lee, K. Watanabe, T. Taniguchi, A. Vishwanath, A. Yacoby, and P. Kim, Andreev Reflection in the Fractional Quantum Hall State, Phys. Rev. X **12,** 021057 (2022).

[31] M. J. Zhu, A. V. Kretinin, M. D. Thompson, D. A. Bandurin, S. Hu, G. L. Yu, J. Birkbeck, A. Mishchenko, I. J. Vera-Marun, K. Watanabe, T. Taniguchi, M. Polini, J. R. Prance, K. S. Novoselov, A. K. Geim, and M. Ben Shalom, Edge currents shunt the insulating bulk in gapped graphene, Nat. Commun. **8,** 1 (2017).

[32] M. T. Allen, O. Shtanko, I. C. Fulga, A. R. Akhmerov, K. Watanabe, T. Taniguchi, P. Jarillo-Herrero, L. S. Levitov, and A. Yacoby, Spatially resolved edge currents and guided-wave electronic states in graphene, Nat. Phys. **12,** 128 (2016).

[33] M. T. Allen, O. Shtanko, I. C. Fulga, J. I.-J. Wang, D. Nurgaliev, K. Watanabe, T. Taniguchi, A. R. Akhmerov, P. Jarillo-Herrero, L. S. Levitov, and A. Yacoby, Observation of electron coherence and Fabry-Perot standing waves at a graphene edge, Nano Lett. **17,** 7380 (2017).

[34] J. Ying, J. He, G. Yang, M. Liu, Z. Lyu, X. Zhang, H. Liu, K. Zhao, R. Jiang, Z. Ji, J. Fan, C. Yang, X. Jing, G. Liu, X. Cao, X. Wang, L. Lu, and F. Qu, Magnitude and spatial distribution control of the supercurrent in Bi_2O_2Se-based Josephson junction, Nano Lett. **20,** 2569 (2020).

[35] M. T. Bell, J. Paramanandam, L. B. Ioffe, and M. E. Gershenson, Protected Josephson Rhombus Chains, Phys. Rev. Lett. **112,** 167001 (2014).

[36] C. Schrade, C. M. Marcus, and A. Gyenis, Protected Hybrid Superconducting Qubit in an Array of Gate-Tunable Josephson Interferometers, PRX Quantum **3,** 030303 (2022).

[37] R. C. Dynes and T. A. Fulton, Supercurrent density distribution in Josephson junctions, Phys. Rev. B **3,** 3015 (1971).

[38] A. Papoulis, *The Fourier Integral and its Applications* (McGraw-Hill Book Company Inc., New York, 1962).

[39] B. H. Elfeky, N. Lotfizadeh, W. F. Schiela, W. M. Strickland, M. Dartiailh, K. Sardashti, M. Hatefipour, P. Yu, N. Pankratova, H. Lee, V. E. Manucharyan, and J. Shabani, Local control of supercurrent density in epitaxial planar Josephson junctions, Nano Lett. **21,** 8274 (2021).

[40] L. Wang, I. Meric, P. Y. Huang, Q. Gao, Y. Gao, H. Tran, T. Taniguchi, K. Watanabe, L. M. Campos, D. A. Muller, J. Guo, P. Kim, J. Hone, K. L. Shepard, and C. R. Dean, One-dimensional electrical contact to a two-dimensional material, Science **342,** 614 (2013).

[41] L. Banszerus, M. Schmitz, S. Engels, J. Dauber, M. Oellers, F. Haupt, K. Watanabe, T. Taniguchi, B. Beschoten, and C. Stampfer, Ultrahigh-mobility graphene devices from chemical vapor deposition on reusable copper, Sci. Adv. **1,** e1500222 (2015).

[42] L. Banszerus, M. Schmitz, S. Engels, M. Goldsche, K. Watanabe, T. Taniguchi, B. Beschoten, and C. Stampfer, Ballistic transport exceeding 28 μm in CVD grown graphene, Nano Lett. **16,** 1387 (2016).

[43] P. Rickhaus, R. Maurand, M.-H. Liu, M. Weiss, K. Richter, and C. Schönenberger, Ballistic interferences in suspended graphene, Nat. Commun. **4,** 1 (2013).

[44] M. Ben Shalom, M. J. Zhu, V. I. Fal'ko, A. Mishchenko, A. V. Kretinin, K. S. Novoselov, C. R. Woods, K. Watanabe, T. Taniguchi, A. K. Geim, and J. R. Prance, Quantum oscillations of the critical current and high-field superconducting proximity in ballistic graphene, Nat. Phys. **12,** 318 (2016).

[45] See Supplemental Material at http://link.aps.org/supplemental/10.1103/PhysRevApplied.20.054049 for details of the current density reconstruction method, a discussion of the measurement setup, and the analysis of Fabry-Perot oscillations.

[46] J. M. Rowell, Magnetic Field Dependence of the Josephson Tunnel Current, Phys. Rev. Lett. **11,** 200 (1963).

[47] W. Albrecht, J. Moers, and B. Hermanns, HNF—Helmholtz Nano Facility, J. Large-Scale Res. Facilities JLSRF **3,** 112 (2017).

[48] https://doi.org/10.5281/zenodo.7632431.